Accepted Manuscript

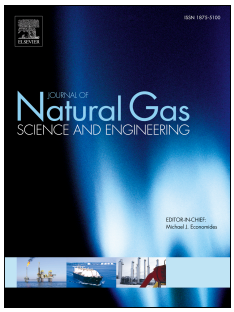

Geochemical modelling of formation damage risk during CO_2 injection in saline aquifers

Min Jin, Ayrton Ribeiro, Eric Mackay

PII: S1875-5100(16)30577-7

DOI: 10.1016/j.jngse.2016.08.030

Reference: JNGSE 1727

To appear in: *Journal of Natural Gas Science and Engineering*

Received Date: 30 March 2016

Revised Date: 27 July 2016

Accepted Date: 11 August 2016

Please cite this article as: Jin, M., Ribeiro, A., Mackay, E., Geochemical modelling of formation damage risk during CO_2 injection in saline aquifers, *Journal of Natural Gas Science & Engineering* (2016), doi: 10.1016/j.jngse.2016.08.030.

Geochemical Modelling of Formation Damage Risk during CO_2 Injection in Saline Aquifers

Min Jin, Ayrton Ribeiro and Eric Mackay*
Heriot-Watt University, Edinburgh, UK
Leonardo Guimarães, Universidade Federal de Pernambuco, Recife, Brazil
**eric.mackay@pet.hw.ac.uk ; +44 131 451 3670*

Abstract

This study provides an understanding of the impact of geochemical reactions during and after CO_2 injection into a potential storage site. The results of calculations of geochemical reactivity of reservoir rock and of cap rock during and after CO_2 injection were performed using a geochemical simulator, with the calculations showing that for these conditions up to 0.5 moles of CO_2 can be dissolved per kg of water. The risk of dissolution of primary cements was considered and identified. In addition, the potential of carbonation reactions to permanently sequester CO_2 was considered, although these reactions were shown to be very slow relative to other processes. The implications for security of storage are that while dolomite nodules exist in the sandstone formation, these do not contribute significantly to the overall rock strength, and hence the risk of dissolution of the formation or caprock causing significant leakages pathways is very low. Further calculations were performed using a commercial reservoir simulation code to account for brine evaporation, halite precipitation and capillary pressure re-imbibition. The impact on injectivity was found not to be significant during continuous and sustained injection of CO_2 at a constant rate. Capillary pressure effects did cause re-imbibition of saline brine, and hence greater deposition, reducing the absolute porosity by up to 13%. The impact of the halite deposition was to channel the CO_2, but for the configuration used there was not a significant change in injection pressure.

1 Introduction

Injection of CO_2 into saline aquifers will cause carbonation of contacted *in situ* brines, disturbing the chemical equilibrium that was established over geological time frames between the brine and the host rock. This may result in dissolution and or precipitation reactions that affect the integrity of the target storage formation rock, the overburden rock, the injectivity of the wells and the security of storage. Continuous injection of dry CO_2 into saline aquifers may also cause the evaporation of the resident brine and eventually lead to formation dry-out in the vicinity of the injector, with associated salt precipitation (André et al., 2007; Giorgis et al., 2007; Pruess, 2009; Qiao et al, 2015). The precipitate may reduce formation effective porosity, permeability, and consequently impact the injectivity.

To investigate these changes, researchers have been using reactive transport simulations using different software packages (Lichtner, 1985; Steefel and Lasaga, 1994; Xu et al., 2011; Nghiem et al., 2011; Parkhurst and Appelo, 2013; Lichtner et al., 2013). A concise explanation and comparison between the available codes can be found in Steefel et al. (2015).

The object of the study is to develop models of carbon dioxide injection into a saline aquifer that includes a detailed mineralogical description of the sandstone formation and a good characterisation of the formation water system, to assess the formation damage near the wellbore and the risk of injectivity impairment by using thermodynamic simulation and geochemical reservoir modelling. The calculations are performed using the PHREEQC thermodynamic model (Appelo and Postma, 2010) and the GEM-GHG reservoir simulation and coupled geochemical code (CMG, 2015a), which has been adapted specifically for use in Green House Gas storage modelling. Using the former, thermodynamic (0D) calculations have been performed to assess the impact of dissolution of CO_2 in the formation water on the reactivity of the primary minerals present in the reservoir, and the precipitation of secondary minerals. Using the later, a 2D reactive transport model was built corresponding to simulations that couple hydrodynamic and geochemical modelling to assess the impact of halite precipitation.

2 CO_2 Storage Injection site

2.1 Geological data

The sandstone formation was deposited in a broad, gradually subsiding offshore basin. The dominant facies type is very fine to fine grained fluvial laminated sandstone. The reservoir is relatively shallow (1000m-1500m) and has been subdivided into three main zones, Sandstone_L1 at the base, Sandstone_L2 in the middle and Sandstone_L3 at the top of the formation.

The rock properties were interpreted by data from wells which are within an area covering 40 x 50 km. The pore volume of the model was calculated based on the depth map of the structural closure. As the modelling focuses on the region near the wellbore, the exact value of the pore volume is not important for the study. Because the injection site is part of connected structural closures, and especially as there is evidence of a subcrop to seabed to the south east of the main structure, a numerical aquifer is required as a boundary condition for the flow modelling.

Table 2-1 Summary of reservoir parameters

Reservoir Parameter	Value	Units
Depth to top reservoir	1020	m
Thickness	200-250	m
Spill point	1460	m
Porosity (average)	20	%
Permeability (average)	260	mD
Datum	1300	m
Reservoir temperature at datum	57.2	°C
Temperature gradient	3.16	°C per 100 m
Reservoir pressure at datum	14.12	MPa
Pressure gradient	0.0115	MPa/m

A summary of the reservoir parameters is given in Table 2-1. The average porosity of the cored area ranges from 17% in the Lower Model to 24% in the Upper Model, with corresponding estimated average permeabilities of 100md to 800md. The average net pore volume is 4.6×10^9 m^3. The

uncertainty workflows calculated the spill point ranges between 1416m to 1533m, the net to gross between 0.752 and 0.986.

There are no significant barriers to horizontal flow. The only impermeable barriers to vertical flow are mudstone beds, and they are thought unlikely to extend laterally for more than around 100m. Most such beds are rather silty, and probably act only as baffles to vertical flow rather than wholly impermeable barriers.

2.2 Geochemical Data

The formation water analysis shows that all water samples were highly saline (TDS 250000 ± 10000 mg/L) sodium chloride dominated brines with significant concentrations of common rock constituents, such as calcium, magnesium and sulphate.

The modelling of CO_2 injection into the high salinity aquifer involves the solution of the component transport equations, the equations for thermodynamic equilibrium between the gaseous and aqueous phases, and the equations for geochemical reactions between the aqueous species and mineral precipitation and dissolution. A fully coupled approach is implemented in the software GEM used for the study to achieve adaptive-implicit multiphase multicomponent flow simulation with phase and chemical equilibrium and rate-dependent mineral dissolution/precipitation (CMG, 2015a).

2.2.1 Geochemical composition of the formation

Overlying the entire system is a halite-dominated evaporitic sequence, referred to as the Halite. The unit is composed mostly of quite coarsely crystalline halite with inclusions and irregular thin beds of anhydrite. The clay present between the sandstone intervals and the Halite is regarded as a playa mudstone throughout, and is referred to as the Clay.

The mineralogy data comes from 15 core plugs; two plugs were from the Halite, four from the Clay and the remaining from the Sandstone intervals, L3, L2 and L1. Sample depths and the corresponding volume fractions are listed in Table 2-2 and shown in Figure 2-1. The average values for each zone are listed at the bottom of the table; these are the values used in the simulation model.

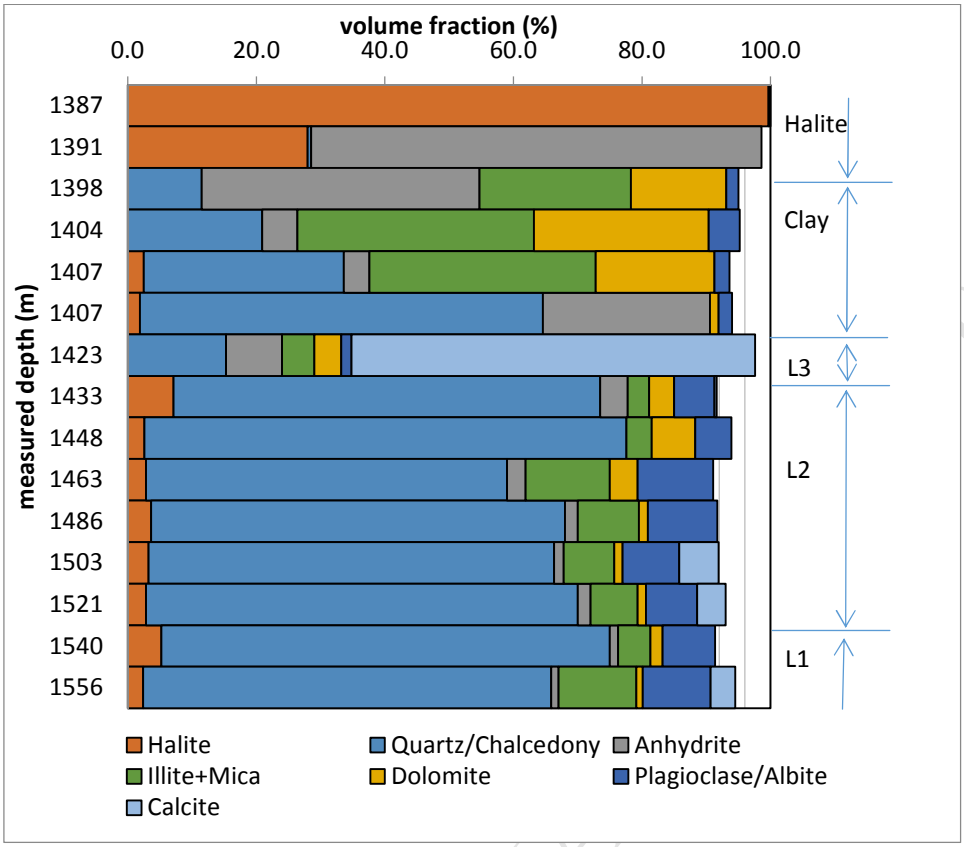

Figure 2-1 Initial major mineral volume fractions (for minerals > 10%) from core analysis.

Table 2-2 Mineral composition of formation from water analysis.

plug	Depth (m)	Illite+Mica*	Chlorite	Quartz	K Feldspar	Plagioclase	Calcite	Dolomite	Magnesite	Halite	Anhydrite	Hematite
1	1387**	0.0	0.0	TR	0.0	0.0	0.0	0.0	0.0	99.7	0.3	0.0
2	1391	0.0	0.0	0.5	0.0	0.0	0.0	0.0	1.4	28.0	70.1	0.0
3	1398	23.6	4.2	11.5	TR	1.9	0.0	14.8	0.0	0.0	43.2	0.8
4	1404	36.8	3.2	20.9	TR	4.8	0.0	27.2	0.0	0.0	5.5	1.6
5	1407	35.2	2.4	31.1	2.2	2.3	0.0	18.5	0.0	2.5	4.0	1.8
6	1408	TR	TR	62.7	5.9	2.1	0.0	1.3	0.0	1.9	26.0	TR
7	1423	5.0	0.7	15.3	0.7	1.6	62.8	4.2	0.0	0.0	8.7	1.1
8	1433	3.3	0.8	66.4	7.1	6.3	0.3	3.9	0.0	7.1	4.3	0.4
9	1448	3.9	0.6	75.0	4.9	5.6	0.0	6.8	0.0	2.6	0.0	0.6
10	1463	13.1	2.1	56.2	4.2	11.8	0.0	4.3	0.0	2.8	2.9	2.6
11	1486	9.5	2.1	64.4	4.4	10.8	0.0	1.4	0.0	3.6	2.0	1.9
12	1503	7.9	1.2	63.1	6.1	8.8	6.1	1.3	0.0	3.2	1.5	0.7
13	1521	7.3	1.5	67.2	4.6	8.0	4.4	1.3	0.0	2.8	2.0	1.1
14	1540	5.0	0.8	69.8	7.1	8.2	TR	1.9	0.0	5.2	1.3	0.7
15	1556	12.1	0.8	63.5	4.0	10.6	3.8	1.0	0.0	2.4	1.1	0.9
	average of L3+L2+L1	7.8		65.7	5.3	8.8	2.1	2.7	0.0	3.7	1.9	1.1
	average of Clay	31.9		21.2	2.2	3.0	0.0	20.2	0.0	0.8	17.6	1.4

*the coloured cells on the heading show the minerals used in the study

** the coloured cells in the column show the formation

Based on the mineralogy analysis in Table 2-2, eight mineral components are chosen as the conceptualization of mineralogy in the geochemical model. They are quartz, illite, calcite, dolomite, K-feldspar, anhydrite, halite, and albite. Among these, albite is used to model plagioclase as the latter is not in the GEM database (CMG, 2015b). The average values in the bottom rows of Table 2-2 are used for the L3+L2+L1 zone and the Clay zone as the input for initial mineral volume fractions.

2.2.2 Formation water composition

Comparing the depth at which water samples were taken for testing (Table 2-3) with the depth where the cores were sampled for mineralogy analysis in Table 2-2 and Figure 2-1, it is found that three water samples match or are close to the core samples, two in Sandstone L1 and L2 (1575 m and 1440 m), one in Sandstone L3 (1412 m) and one in Clay (1400 m). As the thermodynamic model is 0D, and as the 2D radial geochemical model is a homogeneous model, the initial aqueous concentration data were chosen based on the rock and formation water data from the three depths.

Table 2-3 Formation water composition (mg/kg).

	L1	L2	L3	Clay
Sampling Point / Depth (m)	1575	1440	1412	1400
Chloride	154100	148800	148200	155400
Sulphate	300	360	380	360
Bromide	470	460	440	470
Strontium	110	110	100	120
Calcium	8860	8610	8040	9130
Magnesium	2540	3010	3190	3100
Sodium	85500	79700	80000	84800
Potassium	1400	1470	1480	1530
Sulphur	80	100	110	110
Total Dissolved Solids	253360	242620	241940	255020

3 Batch 0D modelling using PHREEQC

It is very useful to run a batch geochemical model to identify the main chemical reactions in the formation and to validate the equilibrium state based on the given water composition data and rock mineral analysis data before building a complex 2D or 3D geochemical model. The batch modelling was performed using the PHREEQC code (Appelo and Postma, 2010).

In total, six sets of calculations were performed using PHREEQC. Initial calculations were performed to identify the initial equilibrium water composition, and how this varied compared to the supplied water composition (although it is evident that great care was taken with sampling and analysis of water, inevitably the process alters the initial equilibrium state, even if the analysis is performed quickly, and thus recalibration of the initial water composition to ensure equilibrium with the primary minerals identified is required). Subsequent calculations then consider the impact of dissolving CO_2 in this brine.

The six sets of calculations correspond to six locations in the sequence at various depths, and their corresponding supplied water compositions. These include three locations within the cap rock (C1,

C2 and C3) and three layers of the reservoir (L1, L2 and L3). All simulations were performed using 1L of water @ 57.2 ℃ and 14.2 MPa. The conditions are identified in Table 3-1

Table 3-1 Selected brine and aquifer sections for PHREEQC simulations.

	Simulation 1	Simulation 2	Simulation 3	Simulation 4	Simulation 5	Simulation 6
Brine Location (m)	1575	1440	1412	1412	1400	1400
Mineralogy Location (m)	1556 (L1)	1448 (L2)	1423 (L3)	1407 (C1)	1398 (C2)	1391 (C3)

The chemical reactions for the PHREEQC modelling were chosen based on the minerals identified in Figure 3-1 and the brine composition. The primary concern is formation damage in the near wellbore zone and the impact CO_2 saturated brine could have on the integrity of the cap rock. For this reason, the precipitation and dissolution of the following minerals was considered in the main thermodynamic modelling activity:

- Dolomite

$$CaMg(CO_3)_{2(s)} = Ca^{+2} + Mg^{+2} + 2 \cdot CO_3^{-2}$$

- Calcite

$$CaCO_{3(s)} = Ca^{+2} + CO_3^{-2}$$

- Anhydrite

$$CaSO_{4(s)} = Ca^{+2} + SO_4^{-2}$$

- Halite

$$NaCl_{(s)} = Na^{+} + Cl^{-}$$

Furthermore, the Pitzer thermodynamic database, which is the most comprehensive database for systems at the pressure, temperature and particularly the salinity of this system, is limited to these reactions.

Table 3-2identifies the change in mineral fractions as a result of the equilibration process, and it may be seen that the changes in all cases are minor. Figure 3-1 shows the new mineral compositions graphically (identifying only minerals that are present in fractions > 10%).

Table 3-2 Equilibrium mineral fractions from PHREEQC simulations.

Simulation 1				Simulation 4		
Mineral	Initial Size Fraction	Final Size Fraction	Delta	Initial Size Fraction	Final Size Fraction	Delta
Anhydrite	1.10%	1.09%	-0.01 p.p.	25.99%	25.99%	<0.01 p.p.
Calcite	3.80%	3.68%	-0.12 p.p.	0%	0%	0 p.p.
Dolomite	0.99%	1.10%	0.11 p.p.	1.30%	1.30%	<0.01 p.p.
Halite	2.40%	1.86%	-0.54 p.p.	1.89%	1.08%	-0.81 p.p.
Quartz	63.50%	63.50%	<0.01 p.p.	62.70%	62.70%	<0.01 p.p.
Simulation 2				Simulation 5		
Mineral	Initial Size Fraction	Final Size Fraction	Delta	Initial Size Fraction	Final Size Fraction	Delta
Anhydrite	0%	0%	0 p.p.	43.19%	43.19%	<0.01 p.p.
Calcite	0%	0%	0 p.p.	0%	0%	0 p.p.
Dolomite	6.79%	6.79%	<0.01 p.p.	14.80%	14.80%	<0.01 p.p.
Halite	2.59%	1.80%	-0.79 p.p.	0%	0%	0 p.p.
Quartz	63.50%	63.50%	<0.01 p.p	11.50%	11.50%	<0.01 p.p.
Simulation 3				Simulation 6		
Mineral	Initial Size Fraction	Final Size Fraction	Delta	Initial Size Fraction	Final Size Fraction	Delta
Anhydrite	8.69%	8.69%	<0.01 p.p.	70.09%	70.09%	<0.01 p.p.
Calcite	62.80%	62.63%	-0.17 p.p.	0%	0%	0%
Dolomite	4.20%	4.35%	0.15 p.p.	0%	0%	0%
Halite	0%	0%	0 p.p.	27.99%	27.50%	-0.49 p.p.
Quartz	15.30%	15.30%	<0.01 p.p	0.50%	0.50%	<0.01 p.p.

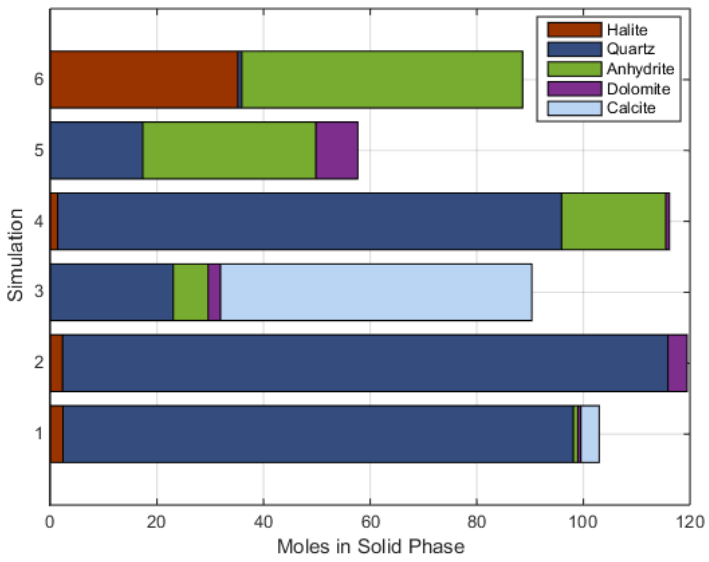

Figure 3-1 Equilibrium mineral fractions from PHREEQC simulations in graphical format.

3.1 CO_2 storage capacity

Having established the initial equilibrium conditions, the next step was to identify the impact of injection of CO_2 in a highly saline brine. This process was broken down into various steps. The first of these steps was to identify the solubility of CO_2 in brine for each of the 6 scenarios. To do this, PHREEQC was used to calculate the solubility of CO_2 in brine at various salinities and temperatures, as shown in Figure 3-2. PHREEQC uses the Peng-Robinson Equation-of-State (EoS) with corrections for high pressure and high salinity to determine the solubility of gases (Appelo et al., 2014; Appelo, 2015).

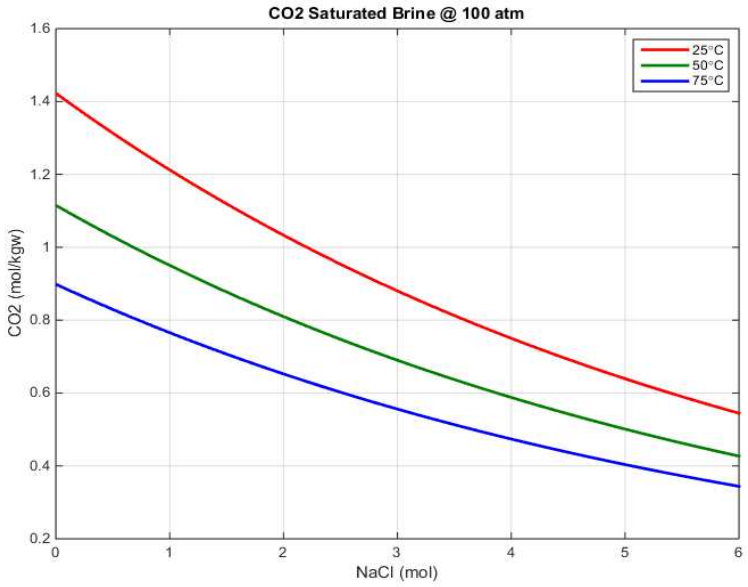

Figure 3-2 Solubility of CO_2 at 10.1 MPa as a function of salinity, calculated by PHREEQC.

The solubility of CO_2 in brine decreases with increasing salinity and with increasing temperature. When 5 mol NaCl is added into 1L of pure water @ 50 ℃ and 10.1 MPa, the maximum concentration of dissolved CO_2 decreases from 1.116 to 0.502 mol/kgw. Therefore, for solutions with more NaCl and other dissolved species the CO_2 solubility is lower than the above value. The temperature effect is not considered further here, but it is worth bearing in mind, since CO_2 will be injected cooler and will then warm up to formation temperature once injected.

The solubility of CO_2 for each of the six scenarios was then calculated, as shown in Figure 3-3.

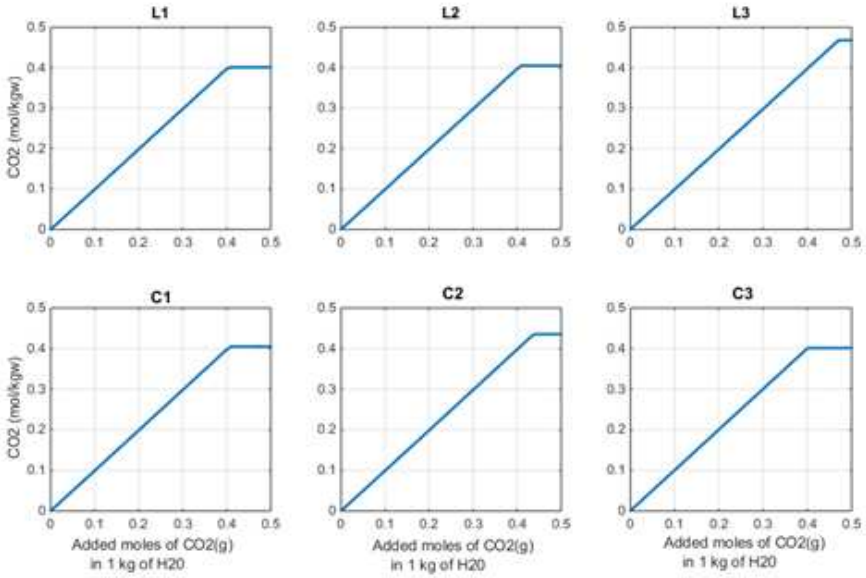

Figure 3-3 Solubility of CO_2 for six scenarios. Maximum saturation can be identified in each case as solubility at which plot becomes horizontal.

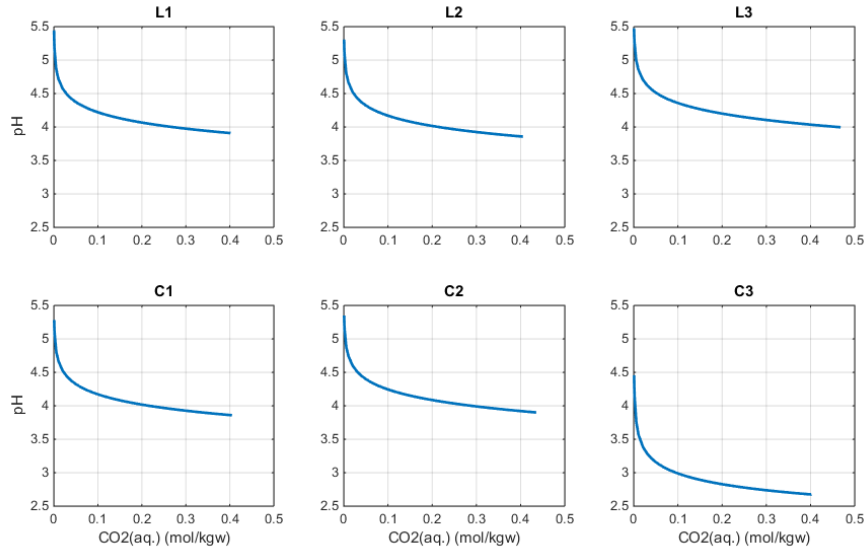

Figure 3-4 pH vs CO_2 concentration for six scenarios. Water becomes more acidic in C3 because of the absence of carbonate minerals.

The CO_2 solubility for the analysed system is between 0.4 and 0.5 mol/kgw for all intervals (around 15000 ppm). The higher saturations in C2, and especially in L3, were achieved because the ion concentrations are significantly lower.

The injection of CO_2 creates carbonic acid, and an important indicator is the resulting pH of the brine. As shown in Figure 3-4, pH decreases for increasing amounts of CO_2 (dissociation of carbonic acid). Lower pH values are reached in C3 because there are no carbonate minerals present to buffer the brine.

3.2 Mineral reactions

Increased concentrations of CO_2 in water trigger dissolution of carbonate minerals. However, we observed (see Figure 3-5) that dolomite was the preferred mineral to dissolve and forced calcite to precipitate in intervals where both minerals were initially present (L1 and L3). Because reactions were coupled in these areas, dolomite dissolution was slightly greater when compared to regions where calcite did not precipitate. Moreover, no net mineralisation of CO_2 is predicted to happen in the reservoir since calcite precipitation was null or lower than dolomite dissolution. In addition, in most simulations anhydrite precipitates, even when carbonate minerals are not present (C3). This precipitation is linked to a continuous increase in overall activity coefficients during CO_2 dissolution in water, which will be explained below.

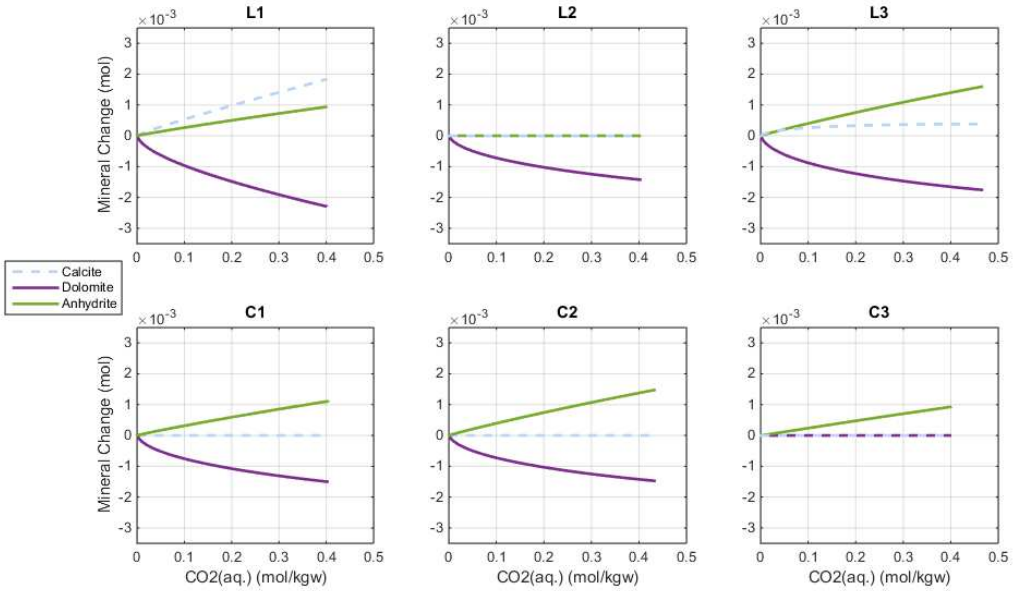

Figure 3-5 Mineral changes resulting from increase in CO_2 concentration for six scenarios, for calcium bearing minerals.

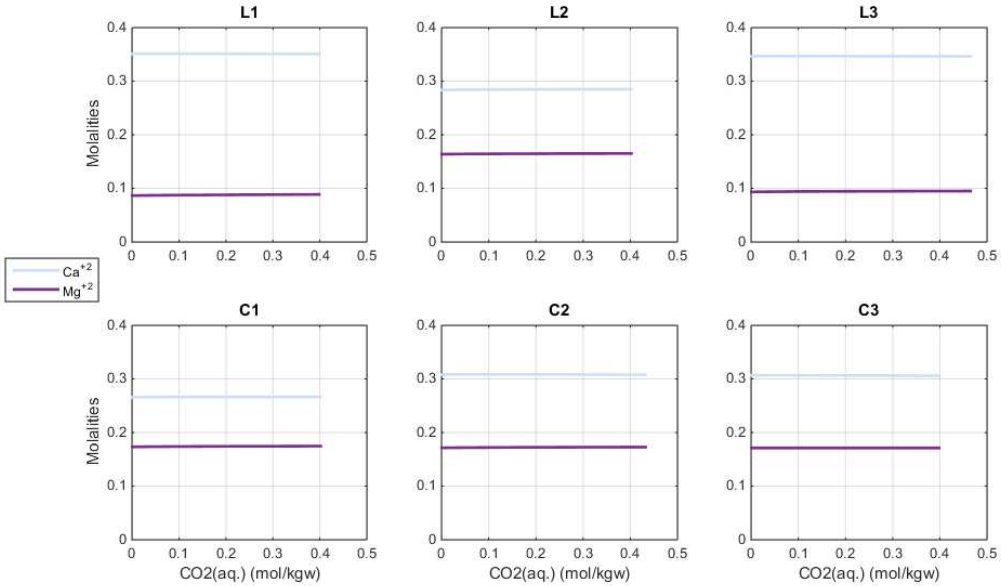

Figure 3-6 Molalities of Ca and Mg vs CO_2 concentration for six scenarios.

The competition between calcite and dolomite for dissolution is related to the Ca/Mg ratio in formation waters (see Figure 3-6) and it can be understood by equilibrating water with both minerals (Appelo, 2013).

$$2 \cdot CaCO_{3(s)} + Mg^{+2} = CaMg(CO_3)_{2(s)} + Ca^{+2}$$

If this reaction is in equilibrium, the following relation holds:

$$K_{dolomte} - (K_{calcite})^2 = \frac{[Ca^{+2}]}{[Mg^{+2}]} = \frac{\gamma_{Ca^{+2}}}{\gamma_{Mg^{+2}}} \cdot \frac{m_{Ca^{+2}}}{m_{Mg^{+2}}}$$

In Figure 3-7, we plotted the apparent (ideal) Ca/Mg mass ratio, i.e. neglecting activity coefficients, for varying temperature and different pressure values. Values above a specific curve indicate the tendency for coupled dolomite dissolution and calcite precipitation.

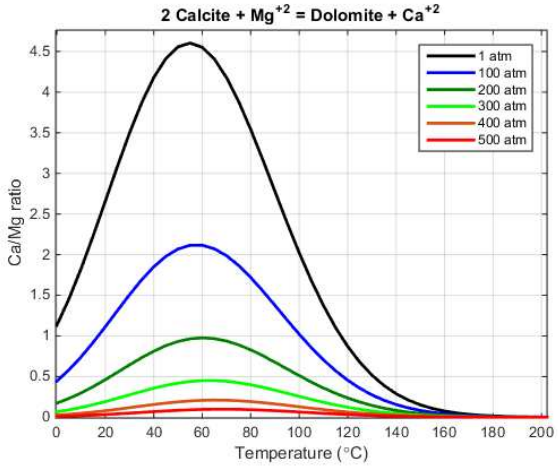

Figure 3-7 Equilibrium Ca/Mg mass ratio (assuming equal activity coefficients) for different pressures and varying temperatures.

Moreover, when observed Ca/Mg ratio is much higher than the equilibrium value, for a given temperature and pressure, means that all dolomite had been previously dissolved and only calcite is left to react. This scenario is observed for different oilfield reservoirs with known water compositions. In addition, with regard to the simulations performed here, calcite precipitation was observed when the apparent SI was high enough.

Table 3-3 Ca/Mg mass ratio in formation water for our simulations and observations from different oilfield reservoirs.

	T (^{o}C)	P (MPa)	Ca (mg/L)	Mg (mg/L)	Ca/Mg	K (mg/L)	App SR	App SI	Mineralogy
Middle Eastern	37	2.3	1279	484	2.6	3.2	0.8	-0.1	Dolomite
C1	57	14.0	10640	4157	2.5	1.5	1.7	0.2	Sand. + Dolomite
L2	57	14.0	11345	3929	2.9	1.5	1.9	0.3	Sand. + Dolomite
C2	57	14.0	12322	4114	3.0	1.5	2.0	0.3	Sand. + Dolomite
C3	57	14.0	12279	4112	3.0	1.5	2.0	0.3	Halite
L3	57	14.0	13861	2239	6.2	1.5	4.1	0.6	Sand. + Limestone
L1	57	14.0	14047	2075	6.8	1.5	4.5	0.7	Sand. + Limestone
Brazilian Pre-salt	60	50.0	22000	4500	4.9	0.09	54.4	1.7	Chalk
Ekofisk	131	48.4	22000	1700	12.9	0.02	645.0	2.8	Chalk
Gyda	160	60.0	30185	2325	12.9	0.002	5863.6	3.8	Sand. + Calcite stringers

Increase in HCO_3 is a consequence of CO_2 dissolution in water. However, in this case most of the HCO_3 is produced by dolomite dissolution, while only a relatively small amount comes from the dissociation of carbonic acid. One can see this by comparing the HCO_3 maximum concentration between C3 (where there are no carbonate minerals) and all the other scenarios (see Figure 3-8). On the other hand, SO_4 decreases when anhydrite precipitates.

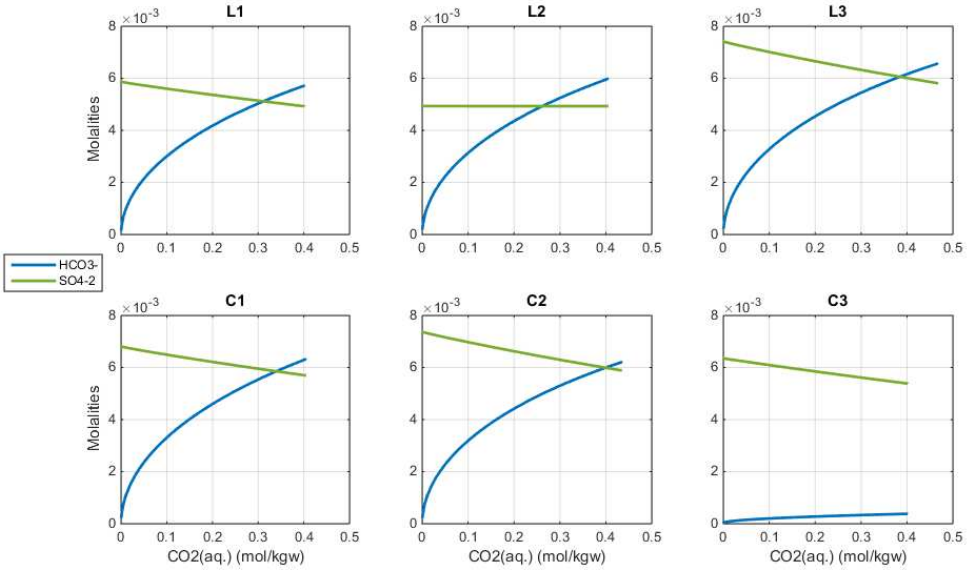

Figure 3-8 Molalities of HCO_3 and SO_4 vs CO_2 concentration for six scenarios.

Furthermore, CO_2 dissolution in water also changes the activity coefficients of species related to mineral reactions. Although the activities of cations generally increase and the activities of anions decrease (see Figure 3-9), the net change is non-zero and therefore the impact of activity on mineral precipitation can be determined by multiplying the coefficients.

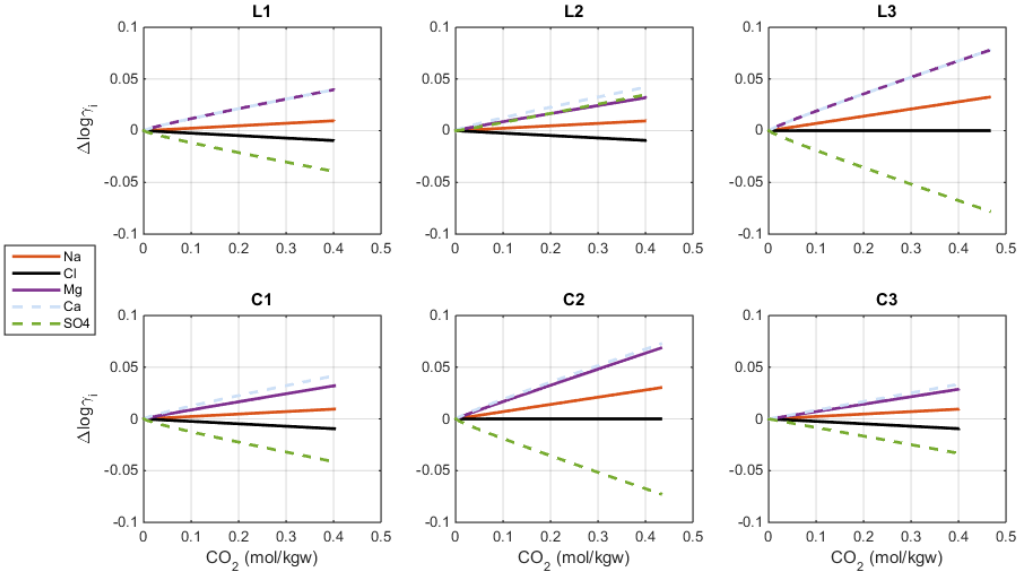

Figure 3-9 Activity coefficients change for representative ions.

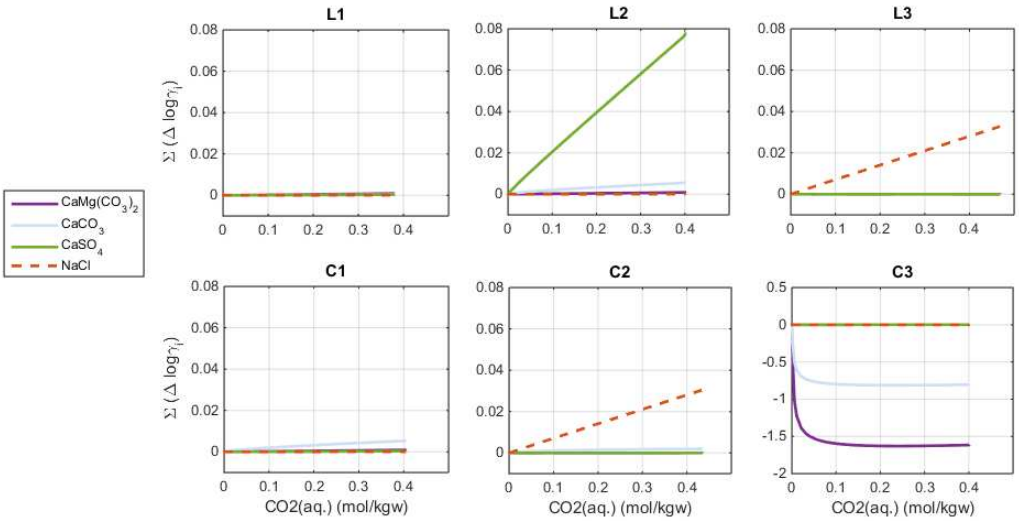

Figure 3-10 Effective change in activity coefficients for each mineral. Large variations indicate undersaturated brines.

One can see in Figure 3-10 that activity coefficients associated with undersaturated minerals change more than the others. The actual dependency is defined by the Pitzer parameters. On the other hand, for reacting minerals, changes in molalities act as constraints on the increase in activity coefficients. In this sense, anhydrite activity shows a steeper increase in L2 because the mineral is not initially present, while for other scenarios the activity increase triggers mineral precipitation which lowers SO_4 molalities and controls the growth of the activity.

Na and Cl, shown in Figure 3-11, are the dominant species and their concentrations set the maximum CO_2 solubility. For areas where halite is initially present, the concentration of these ions decreases because CO_2 dissolution in water triggers halite precipitation by the same mechanism of anhydrite precipitation (see Figure 3-12).

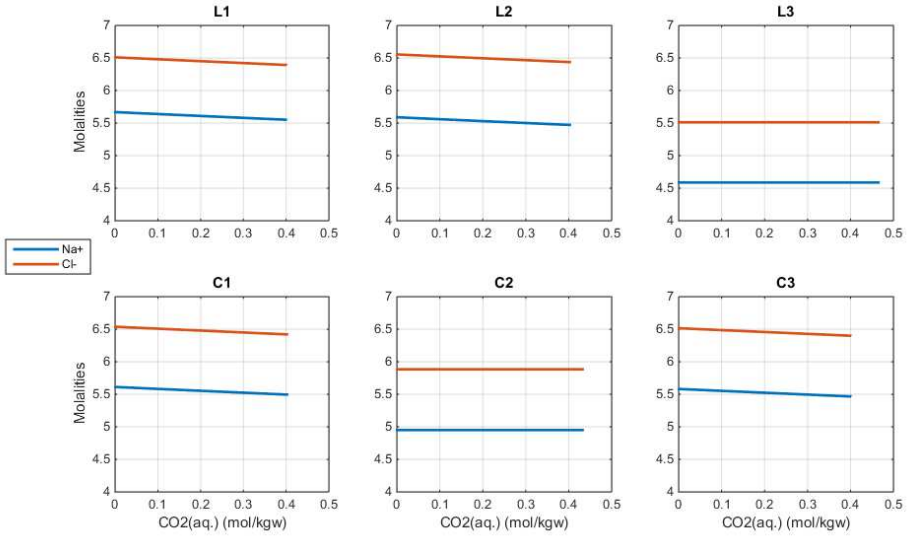

Figure 3-11 Molalities of Na and Cl vs CO_2 concentration for six scenarios.

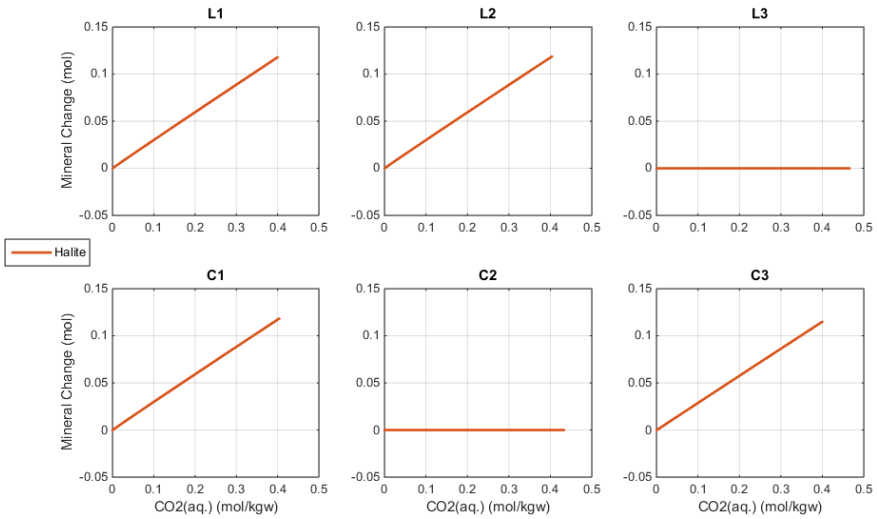

Figure 3-12 Mineral changes resulting from increase in CO_2 concentration for six scenarios, for halite.

3.3 Rock integrity and porosity change

The most significant outcome of these calculations is that only dolomite dissolves in this system – where present – during CO_2 injection. All other minerals will precipitate. The key issue is whether or not dolomite contributes to the integrity of the rock, and if the dolomite is not present as a cement then the risk of formation damage from its dissolution is low**.**

Also of note is the fact that increasing CO_2 concentration will tend to increase the amount of halite precipitation due to evaporation. Moreover, halite precipitation dominates over the others in terms of moles of deposit and in volume change because all analysed minerals have molar volumes of the same order of magnitude. Therefore, if we assume pores completely filled by water, i.e. the porous volume is equivalent to the solution volume, we can estimate the relative changes in porosity ($\Delta\emptyset/\emptyset_o$) due to mineral reactions by dividing the halite volume changes by the PHREEQC solution volumes. As shown in Figure 3-13, the volume change ratio ($\Delta V/V_{Solution}$) associated with halite is in the order of up to $3x10^{-3}$ (precipitation).

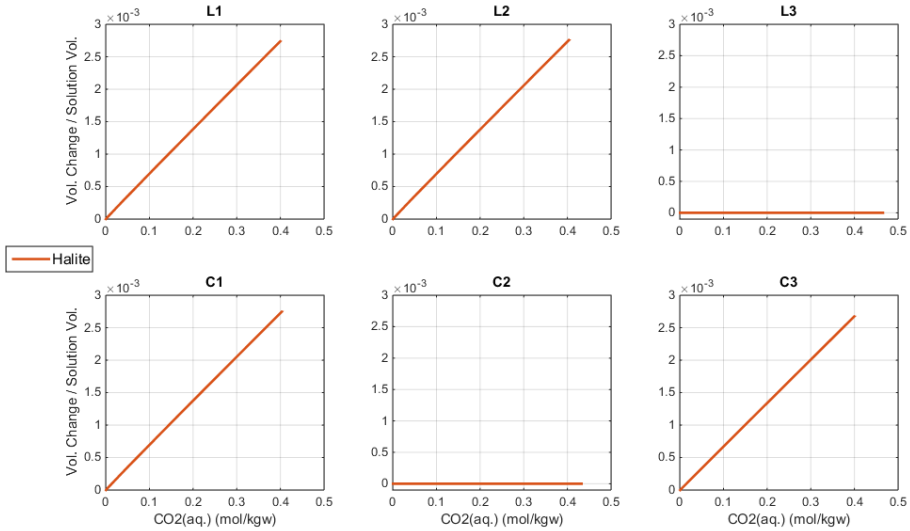

Figure 3-13 Volume changes resulting from increase in CO_2 concentration for six scenarios, for halite. Curves are estimates of relative porosity change.

4 Coupled modelling of fluid flow and geochemical reactions

All simulations in this study were performed using GEM , a general three-dimensional compositional reservoir simulator, using Peng-Robinson EoS (CMG, 2015a).

4.1 Model geometry and properties

Because of computing time constraints due to the multi reactions and multi components in the fluid flow and geochemical coupling simulation, the problem was simplified to a 2D homogeneous model with a radial mesh geometry including 2 layers of cap rock, 45 layers of Sandstone, and one layer of underburden. Two regions were defined to represent cap rock (Halite and Clay) and Sandstone. The underburden has the same properties as the cap rock. The dimensions of the model are 4000 m in radius, 375 m in thickness with a dip angle of 2 degree. The top of the model is at a depth of 1200 m. A numerical aquifer is connected at the outer boundary of the model and the spill point is in the top layer at the outer boundary.

In the 2D model the mesh contains 699 cells in the radial direction and 48 layers in the vertical direction. In the tangential direction there is only one cell with an angle of 360 degree because of the homogeneous and axisymmetric features. The well radius is 0.1 m. The first cell that is connected with the wellbore is 0.1 m in size in the radial direction, and is followed by 642 cells with a constant radial increase of 5m. These are then followed by 57 cells with increments $\Delta Rn+1=c1 \times \Delta Rn$ and c1= 1.03826 until the total radius reaches 4000m.

The injector is in the centre of the model as shown in Figure 4-1. The perforations go through the L2 and L3 zones (layers 22 to 47). Injection of CO_2 is simulated at 0.6 Mt/year for 15 years. A pre-injection run was carried out to establish the formation equilibrium.

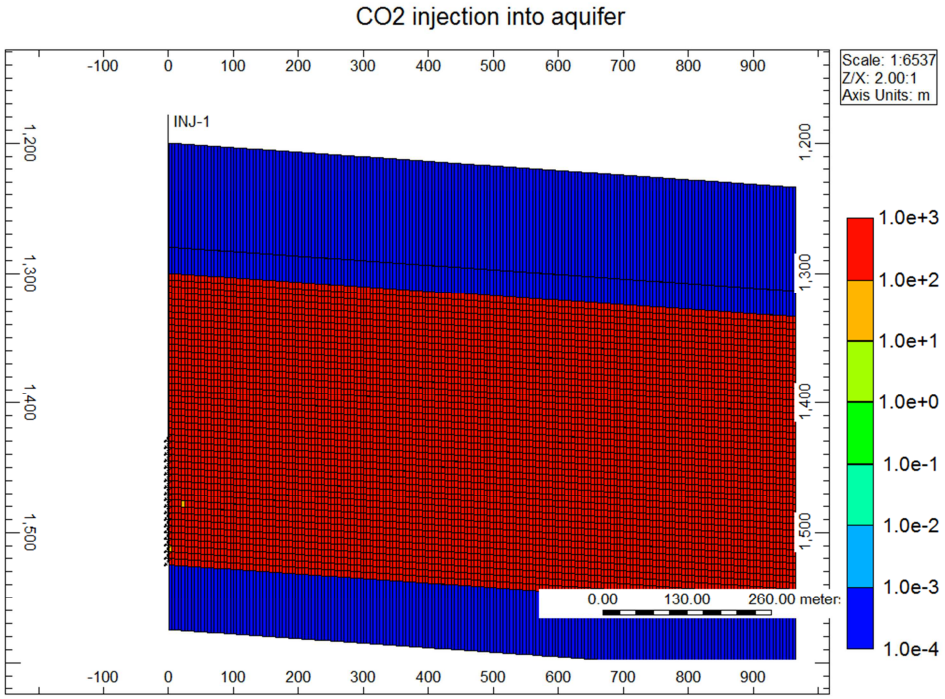

Figure 4-1 The model gridding with permeability contour to show the location of cap rock, formation depth and dip angle, and the well perforation

Figure 4-1 also illustrates the grid top contour on a cross section of the 2D model to show the location of the cap rock, dip angle and the depth of spill point. It can be seen from the figure that the spill point is at the outermost column of cells with the depth of about 1480m. Because a numerical aquifer is connected with the horizontal boundary of the model, CO_2 can migrate to the numerical aquifer with brine.

Viking 2 relative permeability curves (Bennion and Bachu, 2008) and capillary pressure curve were used in the generic model, in which Van Genuchten function (van Genuchten, 1980) was used for the calculation of liquid relative permeability and capillary pressure; Corey function (Corey, 1954) was used for gas relative permeability. The sensitivity study of capillary pressure was performed with low, medium, and high entry pressure (up to 15 MPa).

Table 4-1 Input data for simulation models

Property	Unit	Value
Grid type		2D Radial model
Grid dimension (I x J x K)		699x1x48
datum	m	1300
Pressure	kPa	14120
Pressure gradient	MPa/m	0.0115
Temperature	C	57.2
Temperature gradient	Degree C/m	0.0316
Pore compressibility	1/kPa	$5.0x10^{-7}$
Porosity (o/u burden)	fraction	0.1
Porosity (BSS)	fraction	0.22
Permeability (o/u' burden)	mD	0.0001
Permeability (BSS)	mD	500
Deepest inj. point	m	1459.0
Top perforation	m	1292.0
Pressure change	MPa	1.1 @2019m

In the geochemical and fluid flow coupled simulation the irreducible brine saturation will play an important role in determining the mass of minerals that may dissolve. Therefore, a relative permeability function taken from the cores in the area of interest is very important. As no relative permeability functions were made available at the outset of this study, an assumed function was chosen based on the regional permeability and porosity. Brine properties are a function of brine composition, as discussed in Section 2.

4.2 Thermodynamic data and chemical reactions

The gaseous phase and the aqueous phase are assumed to be in thermodynamic equilibrium. GEM allows a choice of activity model for the aqueous phase: the ideal model, the Debye-Hückel model or the B-dot model. The accuracy of these models reduces for brines with salinities above 2M, but since the more appropriate Pitzer model used in PHREEQC is not available in GEM, the B-dot model was used instead. However, this will introduce some errors relative to the PHREEQC calculations. To check the compatibility between the two different models, we have performed thermodynamic simulations (with no transport) using GEM with B-dot for the data related to Section L1. Figure 4-2 shows the mineral changes for different CO_2 concentrations. One can compare these results with the PHREEQC simulations and see some differences. First, calcite (for high CO_2 concentrations) and anhydrite (entire range) dissolve. Second, the mineral changes in moles calculated by GEM's B-dot are lower than the results from PHREEQC's Pitzer, with the largest difference being associated with halite (more than one order of magnitude). On the other hand, both codes reproduce the precipitation of halite as the dominant mineral reaction. Nevertheless, GEM has the capability of multiphase transport and additional precipitation occurs (because of evaporation) during gas injection, while PHREEQC is limited to unidimensional transport of water only. Moreover, it has been reported that TOUGHREACT, which uses the extended Debye-Huckel activity model (Xu et al., 2011), can produce results similar to PHREEQC and GEM if the same thermodynamic database is used in each of them (Gundogan, 2011). Thus we use GEM as it is at least as good as any other model in

terms of ability to include the impact of both transport and evaporation for the halite deposition calculations, although it is recognised that the activity model used has limitations. However, since the initial concentrations of sodium and chloride are the same for both models, and in the GEM model which accounts for transport and evaporation, such differences are small in the near wellbore region since the majority of the deposited mass is due to the evaporation of the brine, not due to the change in solubility of halite.

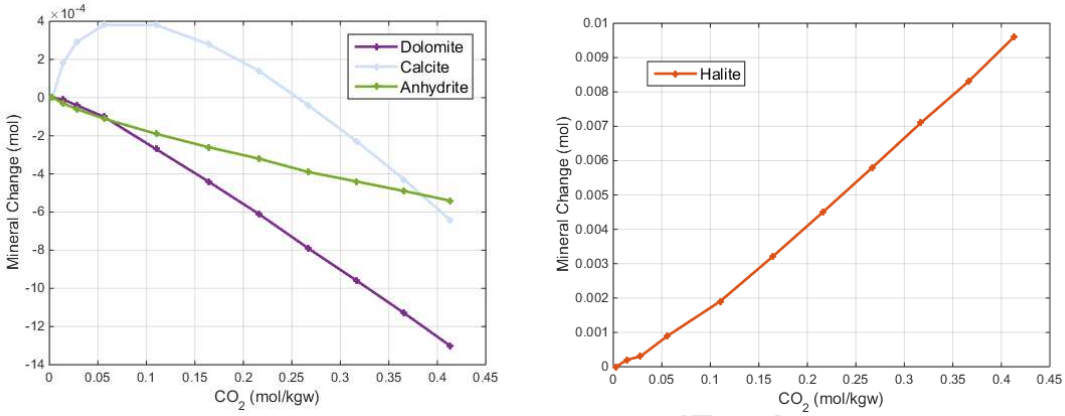

Figure 4-2 Mineral changes (in moles) for section L1 calculated by GEM using B-dot activity model. Static simulations were performed with a reservoir model with 1 L of porous volume saturated with water and different amounts of dissolved CO_2.

Henry's law is used to calculate the fugacity of gaseous components soluble in the aqueous phase. The Henry's constants are functions of pressure, temperature and salinity. The salting-out process includes the phenomenon where the solubility of CO_2 decreases with the increasing salinity. To model H_2O vaporization, which may form a dry zone near the injector and cause a decrease of CO_2 injectivity, a thermodynamic equilibrium of H_2O is applied.

At the same time, chemical reactions take place between minerals and aqueous components (identified as heterogeneous reactions) and among components in the aqueous phase (homogeneous reactions), including gaseous components such as CO_2 that are soluble in the aqueous phase as well as components that exist only in the aqueous phase. Normally intra-aqueous reactions are represented as chemical-equilibrium reactions as they are fast relative to mineral dissolution/precipitation reactions that are represented as rate-dependent reactions. In the following we list the relevant equations that are implemented in GEM.

The rate law for the mineral dissolution and precipitation reaction is (Bethke, 1996):

$$r_\beta = \hat{A}_\beta k_\beta \left(1 - \frac{Q_\beta}{K_{eq,\beta}}\right) \qquad (4\text{-}1)$$

where r_β is the rate, $\hat{A}_\beta$ is the reactive surface area for mineral β, k_β is the rate constant of mineral reaction β, $K_{eq,\beta}$ is the chemical equilibrium constant for mineral reaction β and Q_β is the activity product of mineral reaction β.

The reactive surface area $\hat{A}_\beta$ is another important parameter in the calculation of the rate. Eq 4-2 is used to calculate the reactive surface area with change in the moles of minerals through dissolution or precipitation:

$$\hat{A}_\beta = \hat{A}_\beta^0 \frac{N_\beta}{N_\beta^0} \qquad (4\text{-}2)$$

where $\hat{A}_\beta^0$ is the reactive surface area at time T_0, N_β is the mole number of mineral β per unit grid block volume at current time and $N_\beta{}^0$ is the mole number of mineral β per unit grid block bulk volume at time T_0.

The ratio ($Q_\beta/K_{eq,\beta}$) in equation 4-1 is called the saturation index of the reaction. If ($Q\beta/K_{eq,\beta}$) > 1, mineral dissolution occurs; otherwise, mineral precipitation occurs.

Three aqueous reactions and seven mineral reactions are selected, based on the PHREEQC modelling in Section 3, and reactions reported in the literature for minor minerals. Table 4-2 shows the reactions and kinetic rate parameters used in the modelling with references. The initial aqueous-component concentrations and mineral volume fractions are listed in Table 4-3. As noted above, the choice of activity model for the aqueous phase is not suitable for very high salinity brines, and the brine composition used here has lower overall salinity than that used in the batch modelling above (Section 3).

Table 4-2 Reactions modelled. The first three are aqueous reactions and assumed to be equilibrium. The others are mineral reactions and require kinetic parameters to be specified. (The Na and Cl concentrations will mean that halite precipitation will dominate all other reactions.)

Reaction	Source for values of kinetic parameters
$CO_2(aq)+H_2O = H^+ + HCO3^-$	
$CO_3^{--}+ H^+ = HCO3^-$	
$OH^- + H^+ = 2H_2O$	
Anhydrite = $Ca^{++} + SO_4^{--}$	(Audigane et al., 2005)
Calcite + $H^+ = Ca^{++} + HCO_3^-$	(Noh et al., 2004)
Dolomite + 2 $H^+ = Ca^{++} + Mg^{++} + 2\ HCO_3^-$	(Pokrovsky and Schott, 2001)
Halite = $Na^+ + Cl^-$	(Alkattan et al., 1997)
Illite + $8H^+ = 5\ H_2O + 0.6K^+ + 0.25\ Mg^{++} + 2.3\ Al^{++} + 3.5SiO_2(aq)$	Set to muscovite rate (Nagy, 1995)
K-feldspa + $4H^+ = 2\ H_2O + 0.6K^+ + Al^{++} + 3SiO_2(aq)$	(Nagy, 1995)
Quartz = $SiO_2(aq)$	(Rimstidt and Barnes, 1980)

Table 4-3 Initial input data for aqueous components and mineral components for cap rock and reservoir

Aqueous component	Concentration for cap rock (molality)	Concentration for reservoir (molality)	Mineral component	Concentration for cap rock (volume fraction)	Concentration for reservoir (volume fraction)
H	1.00E-07	1.00E-07	Albite	0.03	0.088
Na	3.6882	3.7196	Anhydrite	0.176	0.019
Al	1.00E-07	1.00E-07	Calcite	0.0	0.021
SiO_2(aq)	1.00E-07	1.00E-07	Dolomite	0.202	0.027
Ca	0.2278	0.2210	Halite	0.008	0.037
SO_4	1.00E-07	1.00E-07	Illite	0.319	0.078
Mg	0.1277	0.1046	K-feldspar	0.022	0.053
Cl	4.3834	4.3479	Quartz	0.212	0.657
K	0.0339	0.0358			
HCO_3	1.00E-07	2.00E-04	Total	0.969	0.980
CO_3	1.00E-07	1.00E-07			
OH	1.00E-07	1.00E-07			

There are two key cut off values to control the chemical reactions in the simulation. The minimum aqueous phase saturation, under which all geochemical reactions, including mineral precipitation/dissolution, will stop, was set to $1x10^{-4}$. The residual aqueous phase saturation for H_2O vaporization, under which the vaporization ceases, was set to $1x10^{-2}$. As the precipitation and dissolution of halite is very rapid, it is often treated by means of a local equilibrium process (Alkan et al., 2010) or by a reaction, but setting the reaction rate to a high value (Noh et al., 2004).

4.3 Porosity-permeability relationship in dynamic simulation

Mineral dissolution and precipitation change the void volume of the porous medium. The porosity, ϕ, altered as a result of mineral precipitation or dissolution is updated in each timestep, and is calculated from the mineral volume fraction at the current time, as follows:

$$\hat{\phi}^* = \phi^* - \sum_{\beta=1}^{n_m} \left(\frac{N_\beta}{\rho_\beta} - \frac{N_\beta^0}{\rho_\beta} \right) \quad (4\text{-}3)$$

$$\phi = \hat{\phi}^* [1 + c_\phi (p - p^*)] \quad (4\text{-}4)$$

where $\hat{\phi}^*$ is the reference porosity including mineral precipitation/dissolution, ρ_β is the mineral molar density, $\phi^*$is the reference porosity without mineral precipitation/dissolution, ϕ is the updated porosity, and c_ϕ is the rock compressibility, p* is the reference pressure (CMG, 2015a).

By using an experimental relationship or analytical models between porosity and permeability, a permeability change induced by mineral dissolution or precipitation can be calculated. There are several published porosity-permeability relationships, such as the commonly used and the simplest power law model, the classical Kozeny-Carman model (Carman, 1956), Verma and Pruess's 'tubes-in-series' model (Verma and Pruess, 1988), and the extended Verma-Pruess model (V-P) (Xu and Pruess, 2004). Only the first two relations are currently included in GEM.

The Kozeny-Carman (K-C) equation is used in the study as follows:

$$Resistante\ Factor\ (rf) = \frac{k}{k_0} = \left(\frac{\varphi}{\varphi_0}\right)^3 \left(\frac{1-\varphi^0}{1-\varphi}\right)^2 \quad (4\text{-}5)$$

where k_0 and ϕ_0 are the initial permeability and porosity, respectively, and the K-C constant is assumed to be independent of porosity.

The extended V-P model is as follows:

$$\frac{k}{k_0} = \left(\frac{\varphi-\varphi_c}{\varphi_o-\varphi_c}\right)^n \quad (4\text{-}6)$$

where ϕ_c is the value of a "critical" porosity at which permeability tends to zero, and n is a power law exponent.

Comparing with the K-C equation, which resulted in a modest decrease in permeability, the V-P model was found more sensitive and more consistent with the observed significant loss of injectivity from field data and lab experiments (Peysson et al., 2011; Xu et al., 2004).

(Graham, 1973) found the permeability to be proportional to $(\phi-\phi_c)^n$, and n=1.8 for sintered metallic powders. (Vaughan et al., 1985) indicated that a mere 8% reduction in original porosity resulted in 96% reduction in permeability of a granite rock core from geothermal laboratory experiments. (Wyble, 1958) conducted an experimental study on the effects of confining pressure on porosity and permeability for three different types of sandstones. Their results can be restated by factoring out pressure, to provide a relationship that is very similar to the V-P model. There are also several types of porosity-permeability models developed from stress-sensitivity studies (Jin, 1999).

The complexity of the problem is due to the variety of geometric properties, such as the size distribution, pore shapes, and connectivity, among the reservoir formations, and the variety of mechanisms that cause porosity changes, such as mechanical deformation which may primarily affect the wider portion of pores, and mineral precipitation or dissolution which may affect the pore throats (Verma and Pruess, 1988). The simple cubic K-C model is based on the assumption of a 'uniform channel'. The 'bottle-neck' effect, that a major permeability reduction occurs due to only a minor reduction in porosity, cannot be accounted for by using the K-C model. Therefore, this model gives the upper bound on permeability reduction. By contrast, as it is unknown where the halite will deposit - in pore bodies and/or pore throats - and whether once precipitated it will be static, mobile, or mobile until hydrodynamically trapped, the extended V-P model represents the lower bound of permeability reduction.

Considering the very high salinity in the system, and the need to identify the risk of formation damage that may be caused by salt precipitation near the wellbore based on field data in similar situations, the permeability reduction was also calculated by using the V-P model for comparison, although it should be recognised that this represents an extreme end member, and in fact any detailed assessment would require appropriate and specific experimental data. The permeability reduction calculations performed in the study in the absence of appropriate and specific experimental data should provide an envelope of possible outcomes.

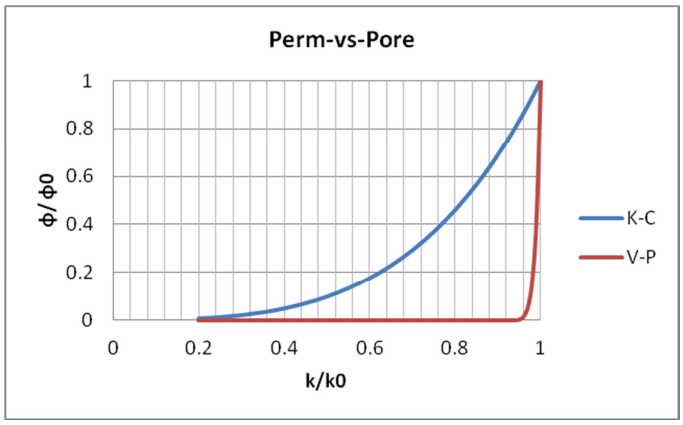

Figure 4-2 comparison of K-C model with V-P model at $\phi_c=0.90\phi_o$ when k=0, and n=8

Because the V-P model is not included in the simulator, a staggered coupling has to be used, i.e. the current permeability, k_n, has to be calculated outside of the program, then the updated value, k_{n+1}, is inputted into the model for the next timestep. The timesteps are 10, 20, 30, 50, 80, 110 days in this study. Thereafter, the property was updated every 1000 days. Critical porosity $\phi_c=0.90*\phi_o$ and n=8 in Eq. 4-6 were used in this staggered simulation. The permeability-porosity relationship is shown in Figure 4-2.

4.4 Discussion of the results from 2D base case model with K-C permeability-porosity model

In this section the results from the base-case model are presented. The output parameters for analysis include porosity change, concentration of halite vs. radial distance and well bottom hole pressure (WBHP) against time. The injector is controlled firstly by CO_2 injection rate, then by WBHP, i.e. if the pressure exceeds the maximum allowed pressure (30 MPa in the study), the injection rate will be reduced. Therefore, the impact of loss of injectivity will be reflected in the pressure change or reduction in flow rate.

Figure 4-3 shows the porosity change due to mineral reactions. As discussed in the previous section, the main porosity change induced by CO_2 injection is from halite precipitation because the concentrations of Na and Cl are so high relative to the other components that halite is the dominant mineral that precipitates during evaporation, and in addition the rates of the other reactions are relatively low.

As shown in Figure 4-3 a low porosity zone was formed gradually at the edge of CO_2 plume. The pronounced vertical solid saturation trend and the emergence of a localized region with very large salt precipitation near the lower portion of the dry-out front was found from a previous study by (Pruess and Müller, 2009) using TOUGH2 simulation, and was noticed by Giorgis et al. (2007). It is caused by a backflow of brine toward to injector under the capillary force, which provides a continuous supply of salt that increases the local salinity and the precipitable solid (Pruess, 2009). Gravity override effects accelerate the accumulation of solids. The edge of the dry-out zone does not move outward due to the buoyancy force acting on the CO_2. A sensitivity study of injection rate was performed and the results are discussed in the next section. As the injection rate in the base case is already very high (0.6 Mt/y), a much higher injection rate (x10, for example) may not be

realistic for the one well in the study. Therefore, a lower injection rate is chosen to provide a comparison with the base case.

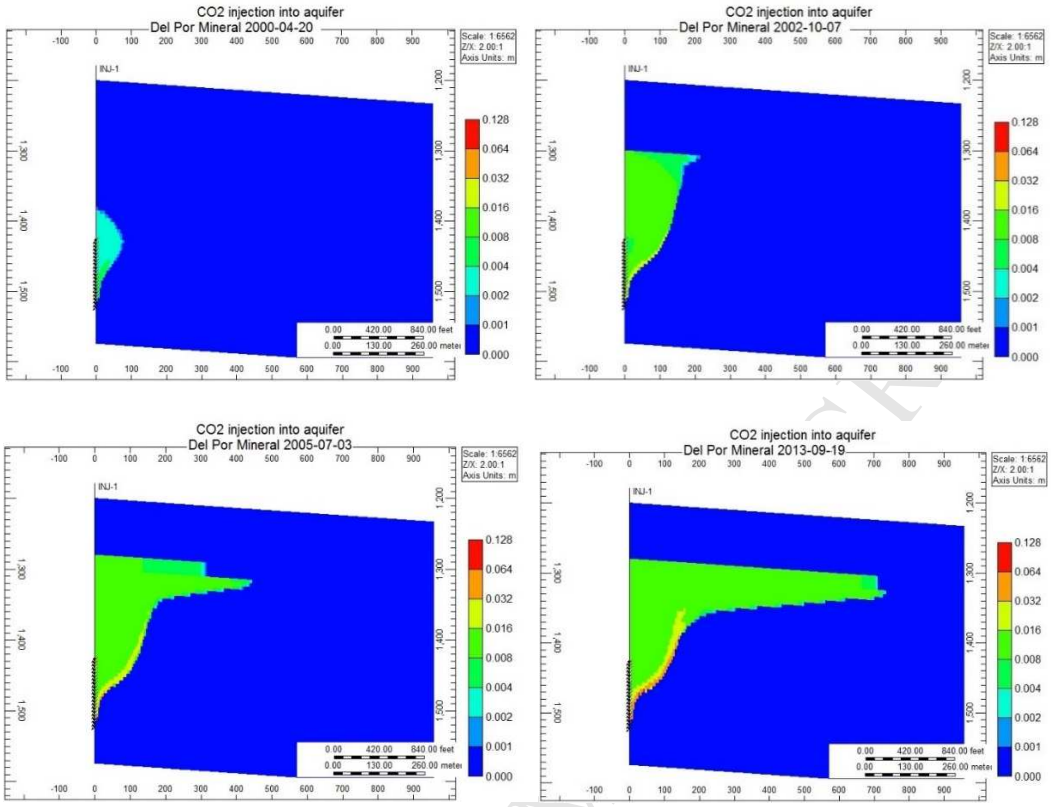

Figure 4-3 Porosity change due to CO_2 injection and salt precipitation at time step = 10, 100, 1000, and 5000 days in the 2D model. The barrier was formed gradually as shown in the figure, and may block the perforations and force a change in the migration path during the rest of the injection period.

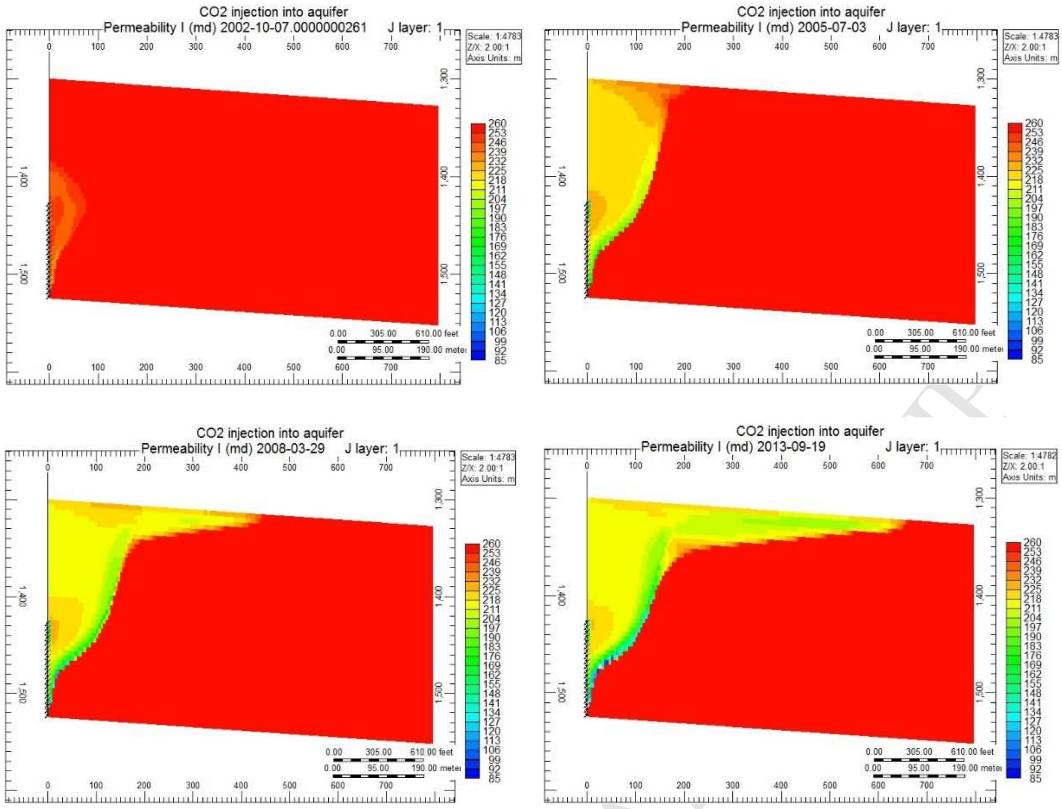

Figure 4-4 permeability reduction due to halite precipitation at different time steps. The permeability in the front at 5000 days reduces to about 1/3 - 1/2 of its initial value. It is also noticeable that the low permeability region is also developed along the perforation at the top of the injection layer.

The permeability reduction due to halite precipitation at different time steps is shown in Figure 4-4. The permeability at the advancing front at 5000 days reduces to about 1/3 to 1/2 of its initial value based on the K-C model. It is also noticeable that a low permeability region is also developed along the top perforations.

Besides the precipitation in the saline aquifer, Figure 4-5 shows the distribution of precipitated halite in the cap rock at 2000 days (left) and 5000 days (right). This may reduce the porosity, and therefore, the permeability in the cap rock, which may improve the sealing capacity of the caprock. The results are from the model with low capillary pressure.

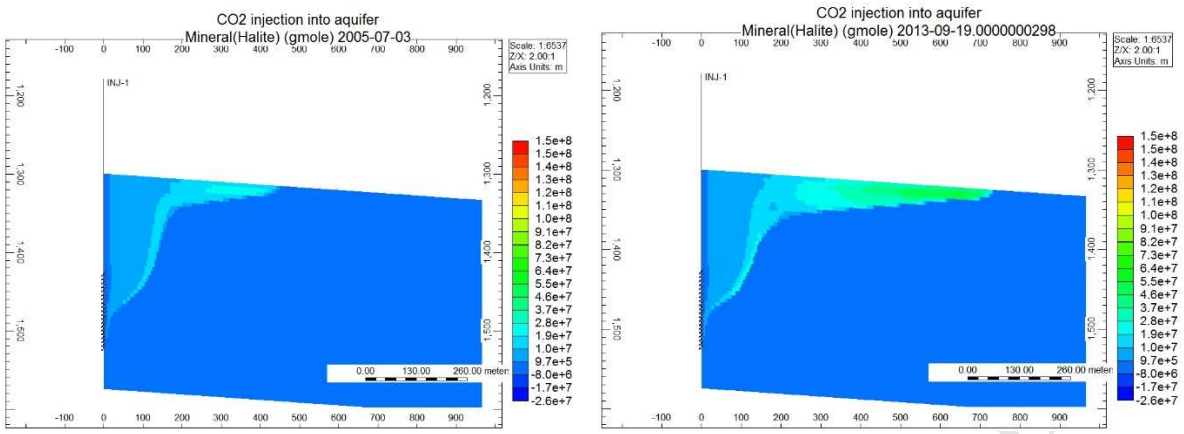

Figure 4-5 the distribution of precipitated halite at 2000 days (left) and 5000 days (right) show that the CO_2 flowing into the cap rock (2000 days after injection in the simulation) may reduce the porosity further, and therefore reduce the permeability of the cap rock. (These results are derived using the model with capillary pressure.)

4.5 Discussion of the results from 2D models with V-P permeability-porosity model

It is worth re-emphasizing that these results represent an extreme end member, with the values being obtained from literature matching silicate precipitation, not halite – and thus they illustrate what damage could be induced in a worst case scenario. A pre-CO_2 injection fresh water flush may be used as a treatment to prevent the damage in the near-well area. In a potential injection site, experimental data for the current system would be required for accurate modelling.

As discussed in Section 4-3, the K-C model cannot be used to represent a sharp permeability decrease as a result of a moderate porosity reduction. Such behaviour can be reproduced by the V-P model, but as this model is not included in the simulator, to use the V-P model in this case the permeability in the simulator is updated after each time step based on Eq. 4-6 with parameters ϕ_c=0.90 ϕ_o and n=8, i.e. when the porosity reduces to 90% of its initial value, the permeability reduces to zero. There is a short time lag between porosity and permeability changes because the permeability at timestep n+1 is calculated based on the porosity at timestep n.

Figure 4-6 and Figure 4-7 show a comparison of the permeability reduction and pressure in the model without fresh water pre-flush (left) and with pre-flush (right) at the same timestep. In the case without the pre-flush, as shown in Figure 4-6 (left), the salt deposition zone gradually surrounds the entire zone where CO_2 can migrate. As a consequence of this flow restriction in the region near the wellbore due to the salt precipitation, the local pressure increases quickly, as shown in Figure 4-7 (left). The pressure within the dry-out zone starts to increase significantly within a two-year injection period.

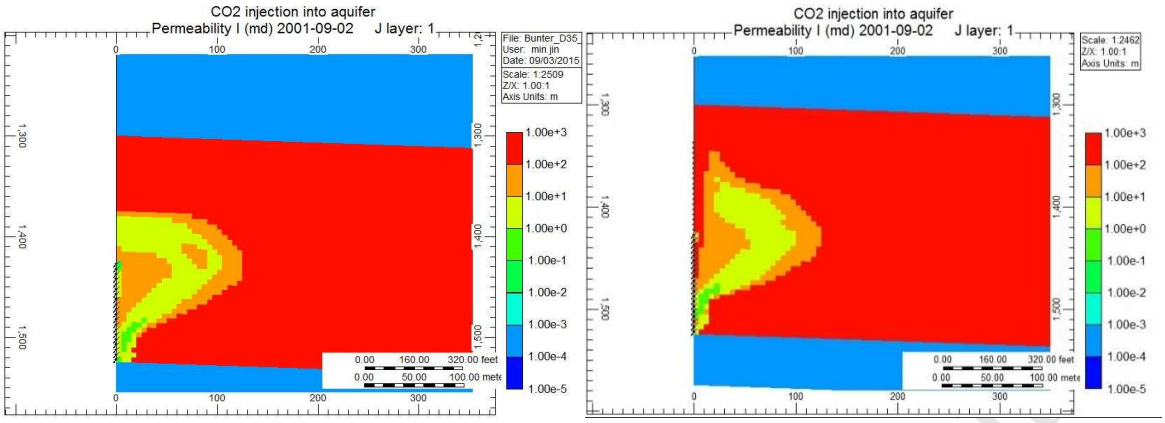

Figure 4-6 permeability distribution after injection of CO_2 for 600 days, left – without fresh water pre-flush, right – with a 10-day pre-injection water flush

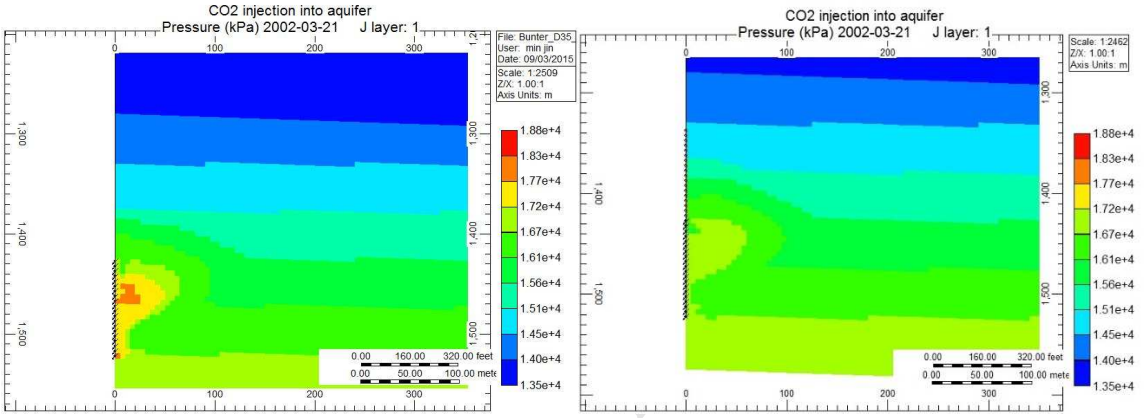

Figure 4-7 pressure distribution after 600 days for models without (left) and with (right) pre-injection fresh water flushing. As a consequence of the deposition zone in the region near the wellbore the local pressure increases quickly.

In the sensitivity study, a freshwater flush is simulated before the injection of CO_2 to reduce the salinity of the brine near the wellbore to reduce the damage caused by salt precipitation in this area. Considering that the greatest porosity reduction occurred in the immediate vicinity of the injection well, and water injection may increase the formation pressure and reduce the capacity of storage if too much is injected, and so the pre-flush is only performed for 10 days at an injection rate of 1000 m^3/day. Comparing the results in Figure 4-6 and Figure 4-7, after this short period of water flush, the low salinity region was sufficient to create a relatively protected zone that permitted CO_2 displacement and pressure release. The maximum well bottom hole pressure value after 3 years injection of CO_2 is reduced by 1280 kPa, about a 40% decrease.

5 Conclusions

The risk of dissolution of primary cements was considered in this study, and it was identified that only dolomite would dissolve under the specified conditions, with all other minerals precipitating. The implications for security of storage are that while dolomite nodules exist in the sandstone, these do not contribute significantly to the overall rock strength, and hence the risk of dissolution of the formation or caprock causing significant leakages pathways is very low.

Mineralisation of CO_2 may occur, but this requires further study, with attention in this work being devoted to the main mineral that precipitates, which is halite. Furthermore, provided dissolution of CO_2 in brine does not create a significant risk of mineral dissolution, the precipitation of minerals will only affect CO_2 already dissolved in the brine phase, and this CO_2 is already very effectively secured due to the greater density of brine saturated CO_2.

The impact on injectivity was found not to be significant during continuous and sustained injection of CO_2 at a constant rate. Capillary pressure effects did cause re-imbibition of saline brine, and hence greater deposition. The impact of the halite deposition was to channel the CO_2, but for the configuration used there was not a significant change in injection pressure, except where extreme modelling assumptions were made.

To make the geochemical simulation more accurate, experiments should be carried out to identify the permeability reduction that will occur due to evaporation in this formation, and to test the change in rock strength and in water composition arising from the contact between the CO_2 saturated brine and the rock. Using such experimental data it would be possible to more accurately identify the impact on injectivity, and remediation opportunities, such as the fresh water pre-flush shown here to have potential, or periodic brine flushes, can be considered in more detail.

6 Acknowledgements

CMG Ltd is thanked for the use of the GEM reservoir simulation model in this work. Foundation CMG are thanked for funding the PhD studentship held by Ayrton Ribeiro and the Chair in Reactive Flow Simulation held by Eric Mackay.

7 References

André, L., Audigane, P., Azaroual, M. and Menjoz, A. (2007). Numerical modeling of fluid-rock chemical interactions at supercritical CO2-liquids interface during CO2 injection into a carbonate reservoir, the Dogger aquifer (Paris Basin, France). *Energy Conversion and Management*, 48, 1782-1797.

Alkan, H., Cinar, Y., and Ülker, E. B. (2010). Impact of Capillary Pressure, Salinity and In situ Conditions on CO_2 Injection into Saline Aquifers. *Transport in Porous Media, 84*(3), 799-819. doi: 10.1007/s11242-010-9541-8

Alkattan, M., Oelkers, E. H., Dandurand, J. and Schott, J. (1997). Experimental studies of halite dissolution kinetics, 1 The effect of saturation state and the presence of trace metals. Chemical Geology, 137, 201-219.

Appelo, C. A. J., and Postma, D. (2010). *Geochemistry, groundwater and pollution* (2nd ed.). The Netherlands: A.A. Balkema Publishers, Leiden, a member of Taylor & Francis Group Plc.

Appelo, C. A. J., Parkhurst, D. L., and Post, V. E. A. (2014). Equations for calculating hydrogeochemical reactions of minerals and gases such as CO2 at high pressures and temperatures. *Geochim. Cosmochim. Acta* 125: 49-67.

Appelo, C. A. J. (2015). Principles, caveats and improvements in databases for calculating hydrogeochemical reactions in saline waters from 0 to 200 °C and 1 to 1000 atm. *Applied Geochemistry* 55: 62 – 71.

Audigane, P., Gaus, I., Pruess, K., and Xu, T. (2005). *Reactive transport modeling using TOUGHREACT for the long term* CO_2 *storage at Sleipner, North Sea*. Paper presented at the Fourth annual conference on carbon capture and sequestration DOE/NETL.

Bennion, D. B., and Bachu, S. (2008). Drainage and imbibition relative permeability relationships for supercritical CO_2/brine and H2S/brine systems in intergranular sandstone, carbonate, shale, and anhydrite rocks. *SPE Reservoir Evaluation and Engineering*(June), 487-492.

Bethke, C. M. (1996). *Geochemical Reaction Modelling*. New York: Oxford University Press.

Carman, P. C. (1956). *Flow of gases through porous media*. London: Butterworth.

CMG. (2015a). User's Guide for GEM Compositional and Unconventional Reserovir Simulator.

CMG. (2015b). *WinProp User Guide for phase-behaviour and fluid property program* C. M. G. Ltd. (Ed.)

Corey, A. T. (1954). The interrelation between gas and oil relative permeabilities. *Producers Monthly*(November), 38-41.

Giorgis, T., Carpita, M., and Battistelli, A. (2007). 2D modeling of salt precipitation during the injection of dry CO_2 in a depleted gas reservoir. *Energy Conversion and Management, 48*(6), 1816-1826. doi: 10.1016/j.enconman.2007.01.012

Graham, R. A. (1973). *A quantitative determination of microstructure on gas permeability of UO2 and Ni sintered bodies.* (M.S.), University of Florida Gaineville, U.S.A.

Gundogan, O. (2011). *Geochemical Modelling of CO2 Storage*. (PhD), Heriot-Watt University, Edinburgh, UK.

Jin, M. (1999). *The numerical modelling of coupled rock mechanics/fluid-flow and its application in petroleum engineering.* (PhD), Heriot-Watt University, Edinburgh, UK.

Lichtner, P. C. (1985). Continuum Model for Simultaneous Chemical Reactions and Mass Transport in Hydrothermal Systems. *Geochimica and Cosmochimica Acta*, Vol. 49, 779-800.

Lichtner, P.C., Hammond, G.E., Lu, C., Karra, S., Bisht, G., Andre, B., Mills, R.T. and Kumar, J. (2013): PFLOTRAN User manual: A Massively Parallel Reactive Flow and Transport Model for Describing Surface and Subsurface Processes.

Nagy, K. L. (1995). dissolution and precipitation kinetics of sheet silicate. In A. F. White and S. L. Barantley (Eds.), *Chemical weathering rate of silicates minerals* (Vol. 31, pp. 173-273): Mineralogical Society of America.

Nghiem, L., Shrivastava, V. and Kohse, B. (2011). Modeling Aqueous Phase Behavior and Chemical reactions in Compositional Simulation. Paper presented in SPE Reservoir Simulation Symposium, The Woodlands, Texas, USA.

Noh, M., Lake, L. W., Bryant, S. L., and Maraque-Martinez, A. (2004). *Implications of coupling fractional flow and geochemistry for* CO_2 *Injection*. Paper presented at the 2004 SPE/DOE Fourteenth symposium on improved oil recovery, Tulsa, Oklahoma, U.S.A.

Parkhurst, D.L. and Appelo, C.A.J. (2013): Description of input and examples for PHREEQC version 3—a computer program for speciation, batch-reaction, one-dimensional transport, and inverse geochemical calculations, U.S. Geological Survey Techniques and Methods, book 6, chap. A43, 497 p., available only at http://pubs.usgs.gov/tm/06/a43

Peysson, Y., Bazin, B., Magnier, C., Kohler, E., and Youssef, S. (2011). Permeability alteration due to salt precipitation driven by drying in the context of CO_2 injection. *Energy Procedia, 4*, 4387-4394. doi: 10.1016/j.egypro.2011.02.391

Pokrovsky, O. S., and Schott, J. (2001). Kinetics and mechanism of dolomite dissolution in neutral to alkaline solutions revisited. *American Journal of Science, 301*, 597-626.

Pruess, K. (2009). Formation dry-out from CO_2injection into saline aquifers: 2. Analytical model for salt precipitation. *Water Resources Research, 45*(3), n/a-n/a. doi: 10.1029/2008wr007102

Pruess, K., and Müller, N. (2009). Formation dry-out from CO_2injection into saline aquifers: 1. Effects of solids precipitation and their mitigation. *Water Resources Research, 45*(3), n/a-n/a. doi: 10.1029/2008wr007101.

Qiao, C., Li, L., Johns, R. T., and Xu, J. (2016). Compositional Modeling of Dissolution-Induced Injectivity Alteration During CO2 Flooding in Carbonate Reservoirs. *SPE Journal*(June). doi:10.2118/170930-PA

Rimstidt, J. D., and Barnes, H. L. (1980). The kinetics of silica-water reactions. *Geochimica et Cosmochimica Acta, 44*(11), 1683-1699.

Steefel, C. I. and Lasaga, A. C. (1994). A coupled model for transport of multiple chemical species and kinetic precipitation/dissolution reactions with application to reactive flow in single phase hydrothermal systems. *American Journal of Science*, 294(5), 529-592.

Steefel, C. I., Appelo, C. A. J., Arora, B., Jacques, D., Kalbacher, T., Kolditz, O., Lagneau, V., Lichtner, P. C., Mayer, K. U., Meeussen, J. C. L., Molins, S., Moulton, D., Shao, H., Simunek, J., Spycher, N., Yabusaki, S. B. and Yeh, G. T. (2015). Reactive transport codes for subsurface environmental simulation. *Computers and Geosciences*, 19, 445-478.

van Genuchten, M. T. (1980). A closed-form equation for predicting the hydraulic conductivity of unsaturated soils. *Soil Science Society of America, 44*(5), 892-898.

Vaughan, P. J., Moore, D. E., Morrow, C. A., and Byerlee, J. D. (1985). The mechanism of permeability reduction during flow of hydrothermal fluids through westerly granite: United States Depertment of the Interior Geological Survey.

Verma, A., and Pruess, K. (1988). Thermohydrological conditions and silica redistribution near high-level nuclear wastes emplaced in saturated geological formations. *Journal of Geophysical Research, 93*(B2), 1159. doi: 10.1029/JB093iB02p01159

Wyble, D. O. W., D.O. (1958). Effect of applied pressure on the conductivity, porosity and permeability of sandstone. *Trans. AIME, 213*, 430-432.

Xu, T., Ontoy, Y., Molling, P., Spycher, N., Parini, M., and Pruess, K. (2004). Reactive transport modeling of injection well scaling and acidizing at Tiwi field, Philippines. *Geothermics, 33*(4), 477-491. doi: 10.1016/j.geothermics.2003.09.012

Xu, T., and Pruess, K. (2004). Numerical simulation of injectivity effects of mineral scaling and clay swellilng in a fractured geothermal reservoir: Lawrence Berkeley National Laboratory.

Xu, T., Spycher, N., Sonnenthal, E., Zhang, G., Zheng, L. and Pruess, K. (2011). TOUGHREACT Version 2.0: a simulator for subsurface reactive transport under non-isothermal multiphase flow conditions. *Computers and Geosciences*, 37, 763-774.

- A 2D geochemical model was built based on both detailed mineralogical analysis and formation water analysis in a potential storage site, and the equilibrium state was validated by PHREEQC. Precipitation of halite around a CO_2 injector, and its possible damage to the formation and solution was studied.
- The risk of dissolution of the formation or caprock causing significant leakages pathways is very low because it was identified from the study that only dolomite would dissolve under the specified conditions, with all other minerals precipitating, and dolomite is only present in some intervals in limited fractions;
- The precipitation of minerals will affect CO_2 already dissolved in the brine phase, and this CO_2 is already very effectively secured due to the greater density of brine saturated CO_2.
- The impact of the halite deposition was to channel the CO_2, but for the configuration used there was not a significant change in injection pressure, except where extreme sensitivity of permeability changes to porosity changes were assumed.
- Further experiments should be carried out to identify the permeability reduction that will occur due to evaporation in this formation, and to provide more accurate models for geochemical simulation and to reduce the uncertainty.